# Multiple Pure Tone Noise Prediction

Fei Han[a], Anupam Sharma[b,*], Umesh Paliath[c], Chingwei Shieh[d]

[a] *Combustion Dynamics & Diagnostics Laboratory, General Electric Global Research Center, 1 Research Circle, Niskayuna, NY, 12309, USA*
[b] *2341 Howe Hall, Department of Aerospace Engineering, Iowa State University, Ames, IA, 50011, USA*
[c] *Aerodynamics & Aeroacoustics Laboratory, General Electric Global Research Center, 1 Research Circle, Niskayuna, NY, 12309, USA*
[d] *Engineering Manager, Engineering Tools Center of Excellence, Greenville, South Carolina, 29601*

**Abstract**

This article presents a fully numerical method for predicting multiple pure tones, also known as "Buzzsaw" noise. It consists of three steps that account for noise source generation, nonlinear acoustic propagation with hard as well as lined walls inside the nacelle, and linear acoustic propagation outside the engine. Noise generation is modeled by steady, part-annulus computational fluid dynamics (CFD) simulations. A linear superposition algorithm is used to construct full-annulus shock/pressure pattern just upstream of the fan from part-annulus CFD results. Nonlinear wave propagation is carried out inside the duct using a pseudo two-dimensional solution of the Burgers' equation. Scattering from nacelle lip as well as radiation to farfield is performed using the commercial solver ACTRAN/TM. The proposed prediction process is verified by comparing against full-annulus CFD simulations as well as

*Corresponding author

*Email addresses:* hanf@ge.com (Fei Han), sharma@iastate.edu (Anupam Sharma), paliath@ge.com (Umesh Paliath), shieh@ge.com (Chingwei Shieh)

against static engine test data for a typical high bypass ratio aircraft engine with hardwall as well as lined inlets. Comparisons are drawn against nacelle unsteady pressure transducer measurements at two axial locations, as well as against near- and far-field microphone array measurements outside the duct.

This is the first fully numerical approach (no experimental or empirical input is required) to predict multiple pure tone noise generation, in-duct propagation and far-field radiation. It uses measured blade coordinates to calculate MPT noise.

*Keywords:* multiple pure tones, Buzzsaw noise, shock noise

## 1. Introduction

Multiple pure tone (MPT) noise, also referred to as “buzzsaw” noise, is generally observed in high-bypass aircraft engines when flow velocity relative to fan blades becomes supersonic near blade tips. It is a common source of annoyance to the cabin passengers and crew. MPT noise is characterized by multiple tones at frequencies that are harmonics of engine shaft frequency (sub harmonics of blade passing frequency). When the blade relative flow velocity becomes supersonic near the blade tip, the rotor-locked pressure field can propagate in the duct and radiate out through the inlet. At subsonic speeds, this rotor locked field decays exponentially with upstream distance. In a hypothetical fan blade where all blades are identical, identically repeating (in blade passing time) pressure pattern would be observed, which would result in noise at the fundamental and the harmonics of the rotor blade passing frequency. However, due to minor blade-to-blade variations (due either to manufacturing or installation), the pressure (shock) pattern is irregular and sub-harmonics of the rotor blade passing frequency are also generated. The whole pressure pattern still repeats after each rotor revolution and hence periodicity with shaft rotation rate is maintained. Therefore, tones at engine (or shaft) order harmonics are observed. Due to the non-linear propagation of these large-amplitude pressure waves, the irregularities in pressure pattern grow as the disturbance propagates upstream in the inlet duct. More and more energy from the blade passing harmonics gets transferred into the engine order tones due to nonlinear propagation. The variation in blade-to-blade stagger angles is known [1, 2] to be the dominant geometric feature that determines the strength of the MPTs generated. Stagger angle differences as small as 0.1 degrees can result in substantial MPT noise generation [2].

MPT noise is typically most severe around cut-back engine speed during the climb phase of a flight. It mostly impacts the passengers and crew that are seated ahead of the engines in the cabin. The noise is quite distinctive and is identifiable due to its striking similarity with noise from a circular buzzsaw. Figure 1 plots a schematic of a fan operation map. In the "started" state, each fan blade has a weak oblique shock at the leading edge and an in-passage shock close to the trailing edge. As the back pressure increases, the in-passage shock moves upstream through the passage and, after a critical value of the back pressure, the in-passage shock merges with the leading edge shock to form a strong bow shock. The fan is then in the "unstarted" state. This is when the MPT signature is the strongest. Typical contour plots of pressure to illustrate the difference in shock strength and position for a fan in the "started" and the "unstarted" states are shown in Fig. 2. As can be seen from Fig. 2, the in-passage, normal shock is swallowed into the passage in the “started” state, while in the “unstarted” state, there is a single, strong, leading edge bow shock per blade. The point, marked ‘P’ in Fig. 1, where the operating line and the ‘start-unstart boundary’ crossover, determines the design speed at which the fan will switch from the “started” to the “unstarted” state during cut-back and lead to generation of MPTs.

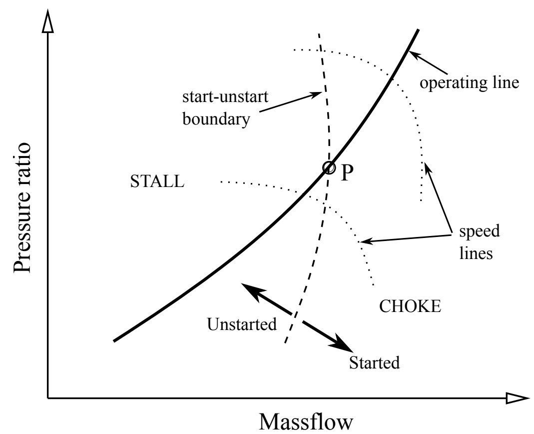


Figure 1: Typical fan map (courtesy Gliebe *et al.* [2]).

(a) “Started”

(b) “Un-started”

Figure 2: Started and unstarted states of a fan shock system.

Several articles [1, 3, 4, 5, 6, 7] have investigated the problem of multiple pure tone noise generation and propagation since the 1970s. Towards predicting MPT noise, Morfey and Fisher [8] calculated the non-dimensional "time of flight" of a wave spiraling around a duct in terms of the axial distance upstream of the fan, as well as the nonlinear attenuation of a regular sawtooth waveform. McAlpine and Fisher [9] proposed both time domain and frequency domain numerical solution methods to study nonlinear propagation of irregular sawtooth waveform. The frequency domain method was later extended to include liner attenuation effects [10] and validated against engine test data [11, 12]. Another approach, based on the modified Hawkings formulation, was developed by Uellenberg [13] to account for arbitrary initial waveform spacings. In all the prediction studies mentioned above, the authors either assumed the initial irregular waveform or took measured data as initial solution and studied only the nonlinear propagation of such waveform as it propagates upstream inside a duct. Other researchers have studied the shock wave generation and propagation of transonic fan blades with the use of CFD [14, 15, 16]. However, they assumed identical fan blade geometries in their numerical calculations and could only analyze nonlinear propagation and decay of shock waves at BPFs but not MPTs.

This article presents an integrated numerical methodology for predicting MPT noise from an engine with measured (through the use of a co-ordinate measuring machine, CMM) blade-to-blade stagger variations. The methodology permits calculation of (a) noise source at the fan face, (b) in-duct propagation with hard- and lined-walls, and (c) radiation out through the inlet to the aircraft fuselage (far field).

## 2. Prediction Process

A summary of the proposed MPT prediction process is provided below. Each of the steps are described in detail in the following sections.

1. Firstly, the irregular pressure pattern just upstream of the fan is computed by solving the Reynolds-Averaged Navier-Stokes (RANS) equations in the frame of reference attached to the fan blade. This can be achieved by carrying out a full-annulus CFD calculation of the entire fan bladerow incorporating the geometric variations in the fan blades as would be observed in the engine during "hot" (running) conditions. Note that this is not straightforward even if the as-manufactured blade geometries are available as one would need to compute the transformation of such variations from "cold" (stationary blades that a CMM would measure) to "hot" conditions. Such full-annulus calculations, in practice, are still too computationally intensive for design purposes. Besides, a designer would typically want to evaluate several permutations of blade ordering in a fan bladerow to minimize MPT noise. A computationally inexpensive procedure to evaluate such combinations is therefore desirable. An approach proposed by Gliebe *et al.* [2] is used where two part-annulus simulations are linearly combined to calculate the contribution of each modified blade passage to the overall engine MPT signature. Linearity with blade stagger is then assumed to obtain the contribution from all the blade passages in the bladerow to get the complete MPT signature from the fan. While the linearity assumption may appear too crude for an essentially nonlinear phenomenon, this article demonstrates through numerical experiments that it works

remarkably well for deviations in blade stagger angles as large as 0.2 degrees (typically deviations observed in engine fan blades are less than this value).

2. The pressure pattern obtained in step 1 just upstream of the fan is next propagated through the engine inlet using a method due to McAlpine and Fisher [9, 10], where the one-dimensional Burgers' equation is solved in the frequency domain. The pressure pattern obtained in step 1 provides the initial condition for the initial value problem that is solved by marching in time using an adaptive time stepping Runge-Kutta solver. The implicit assumption in this approach is that for each azimuthal mode, $m$, only the lowest radial order mode $[m, 0]$ contains all the acoustic energy [9], which does not scattered into higher order radial modes during the propagation. The advantage of the approach is that it is very fast and it also allows treatment of lined walls.

3. As the pressure pattern propagates through the inlet, it decays due both to nonlinear dissipation and absorption of acoustic energy by liners, if present. By the time the pressure pattern reaches the lip of the inlet duct, the amplitudes are considered to be damped enough for the linearity assumption to hold for subsequent analysis. Linear propagation and far-field radiation outside the nacelle is calculated using the commercial solver ACTRAN/TM. Solution is sought for acoustic velocity potential using a conventional finite element method (FEM) inside the computational domain and an infinite element method in the unbounded far-field domain [17].

The above steps are described in detail in the following sections.

## 3. Step #1: Source Prediction

The General Electric (GE) company's in-house computational fluid dynamics (CFD) solver, TACOMA [18, 19] is used for all the RANS solutions used in this article. TACOMA is based on a multi-block, structured, cell-centered, second-order spatial accurate finite volume scheme, with a three-stage Runge-Kutta method for time integration. A two-equation $k-\omega$ turbulence closure model is used to simulate fully-turbulent flows. Fully turbulent flow assumption is made in all the simulations presented in this paper.

As suggested in the previous section, CFD simulations are carried out for part-annulus domains and then combined, assuming linearity, to predict MPT noise. The center blade is staggered 0.2 degrees relative to the other blades. The part-annulus domain has to be large enough to minimize the interaction of the modified shock with itself due to the periodic boundary condition in the circumferential direction. Based on Gliebe *et al.* [2], six blade passages are simulated for the part-annulus calculations.

The linear superposition algorithm by Gliebe *et al.* [2] assumes that MPT noise from a full engine is a linear sum of the contributions from all blade passages, each passage operating individually and independently of the others. Pressure is assumed to vary linearly with blade-to-blade stagger variation.

Consider a hypothetical bladerow in which one blade is slightly out of alignment. Express the perturbed (with circumferentially averaged value removed) pressure field due to this bladerow as spatial Fourier coefficients,

$$p'(\theta) = \sum_{m=-\infty}^{\infty} C_m \exp(im\theta), \tag{1}$$

where, $C_m = C_{mR} + iC_{mI}$ are complex, $i = \sqrt{-1}$, and $C_0 = 0$ because the mean value has been removed.

Changing the stagger of one blade changes the throat area of the two passages neighboring the blade. The shock strength and location depends critically on the passage throat area, and hence we identify below the contribution due to the change in the throat area of one passage. The total perturbation field, $p'(\theta)$ is the sum of the contributions from the two passages ($p'^{(1)}(\theta)$ and $p'^{(2)}(\theta)$), therefore

$$p'(\theta) = p'^{(1)}(\theta) + p'^{(2)}(\theta). \tag{2}$$

Linearity assumption is made to assert that the change in throat area of one passage is equal and opposite to the change in throat area of the other passage. Further assuming that the perturbation pressure field is proportional to the throat area gives the relation

$$p'^{(2)}(\theta) = -p'^{(1)}(\theta) \times \exp(i\delta\theta), \tag{3}$$

where $\exp(i\delta\theta)$ accounts for the phase shift due to the separation in $\theta$ of the two passages ($\delta\theta = 2\pi/B$, where $B$ is the number of fan blades). Equations 2 and 3 give

$$p'(\theta) = p'^{(1)}(\theta)\left\{1 - \exp(i\delta\theta)\right\}, \tag{4}$$

which gives the following relation between the Fourier coefficients of $p'(\theta)$ and $p'^{(1)}(\theta)$

$$\left\{ \begin{array}{c} C_{mR} \\ C_{mI} \end{array} \right\} = \left[ \begin{array}{cc} 1-\cos(\delta\theta) & \sin(\delta\theta) \\ -\sin(\delta\theta) & 1-\cos(\delta\theta) \end{array} \right] \left\{ \begin{array}{c} C^{(1)}_{m\ R} \\ C^{(1)}_{m\ I} \end{array} \right\}, \tag{5}$$

or,

$$\left\{ \begin{array}{c} C^{(1)}_{m\ R} \\ C^{(1)}_{m\ I} \end{array} \right\} = \frac{1}{2} \left[ \begin{array}{cc} 1 & -\cot(\delta\theta/2) \\ -\cot(\delta\theta/2) & 1 \end{array} \right] \left\{ \begin{array}{c} C_{mR} \\ C_{mI} \end{array} \right\}. \tag{6}$$

Using these coefficients, the total pressure field due to the full set of blades with prescribed stagger variations can be constructed by scaling these by the passage variation for each blade passage and summing over all passages.

In the previous analysis by Gliebe *et al.* [2], the authors did not comment on the issue of matching the phase of the pressure signals at the interface boundary between the single- and multi-passage CFD results. This correction is required since the shock waves from the fan are not orthogonal to the passage boundaries and hence while the shocks from modified passages are in the middle at the fan face, they may reach the periodic boundary of the part-annulus simulation further upstream. When combining the single- and multi-passage solutions, one has to ensure that the shocks from the modified blade passages remain in the center. If such phase matching is not performed, as shown schematically in Fig. 3a, an artificial discontinuity in the pressure distribution is created. This can introduce significant errors throughout the spectra (Fourier transform of a step function decays very slowly with frequency). These errors are avoided by shifting the phase of the pressure signal from the multi-passage CFD solution to ensure phase continuity at the interface. The result of the pressure signal reconstruction after phase matching is shown in Fig. 3b.

The linear superposition model is validated against a full-annulus, 2-D RANS simulation for a prescribed (hypothetical and arbitrary) distribution of stagger angles shown in Fig. 4. The pressure field computed for the "started" and the "unstarted" states of the fan shown in Fig 5. Quantitative comparisons between the full-annulus results and the reconstructed pressure field using the procedure outlined above are plotted in Fig. 6. Comparisons are

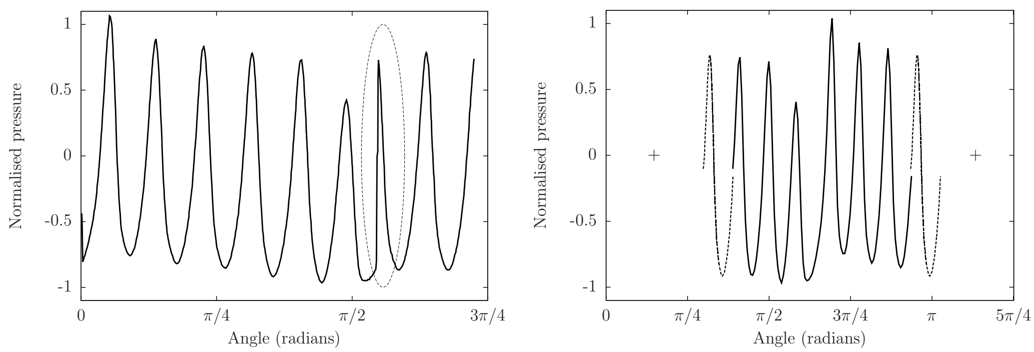


(a) Phase un-matched (b) Phase matched

Figure 3: Spatial variation of pressure obtained by combining six-passage and one-passage simulations when (a) phase matching is not performed, and (b) phase matching is performed. The artificial pressure jump in (a) introduces errors in all frequencies.

made at four different axial positions upstream of the fan blade. The importance of phase correction (matching) during the linear superposition is evident in Fig. 6, where the results obtained both with and without phase matching are compared.

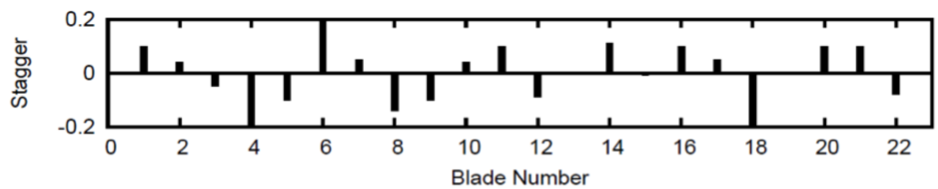


Figure 4: The (arbitrarily chosen) distribution of stagger angles (in degrees) used for the full annulus 2-D simulation.

## 4. Step #2: In-Duct Propagation

In-duct propagation of MPT noise is carried out for both hard-wall as well as lined-wall ducts. For completeness, this section summarizes the pseudo

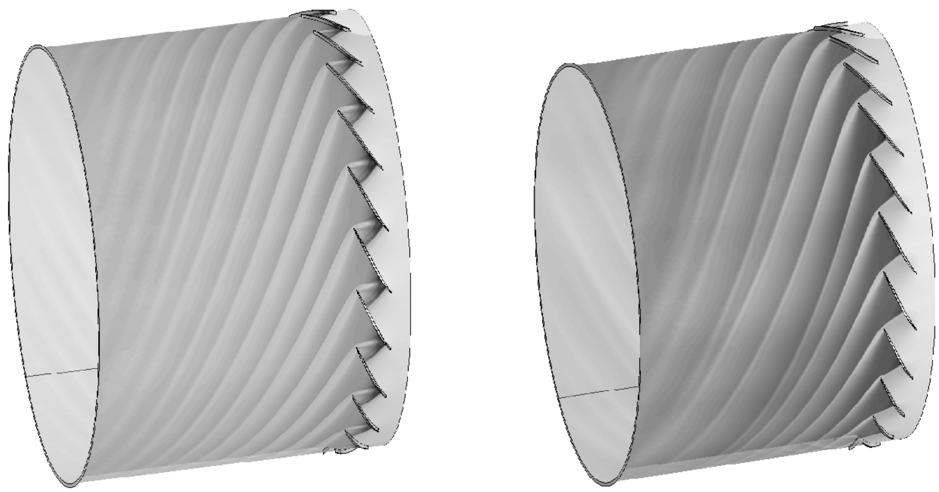

(a) "Started" condition (b) "Unstarted" condition

Figure 5: Two-dimensional, full annulus simulations with specified stagger variation of blades to predict MPT generation in a fan in (a) "started" condition, and (b) "unstarted" condition.

2-D method by McAlpine and Fisher [9] to calculate nonlinear propagation of MPTs in cylindrical ducts. Following [9], we write the nonlinear wave propagation equation in the frequency domain as

$$\frac{\mathrm{d}C_m}{\mathrm{d}T} = \frac{im\pi}{B}\left(\sum_{l=1}^{m-1} C_{m-l}C_l + 2\sum_{l=m+1}^{\infty} C_l\tilde{C}_{l-m}\right) - \epsilon\frac{m^2}{B^2}C_m - \sigma_m C_m, \qquad (7)$$

where, $m$ is the harmonic number of the shaft frequency as well as the azimuthal order of the acoustic mode (this is because the pressure pattern is locked with the rotor), $C_m$ is the complex amplitude of the $m^{th}$ harmonic (of shaft frequency) tone, $T$ is the non-dimensional time, $B$ is the number of fan blades, $\epsilon$ is a dissipation factor to account for the energy lost by the nonlinear dissipation in the frequencies that are ignored due to truncation, and $\sigma_m$ is a damping factor to model the attenuation effect of the acoustic

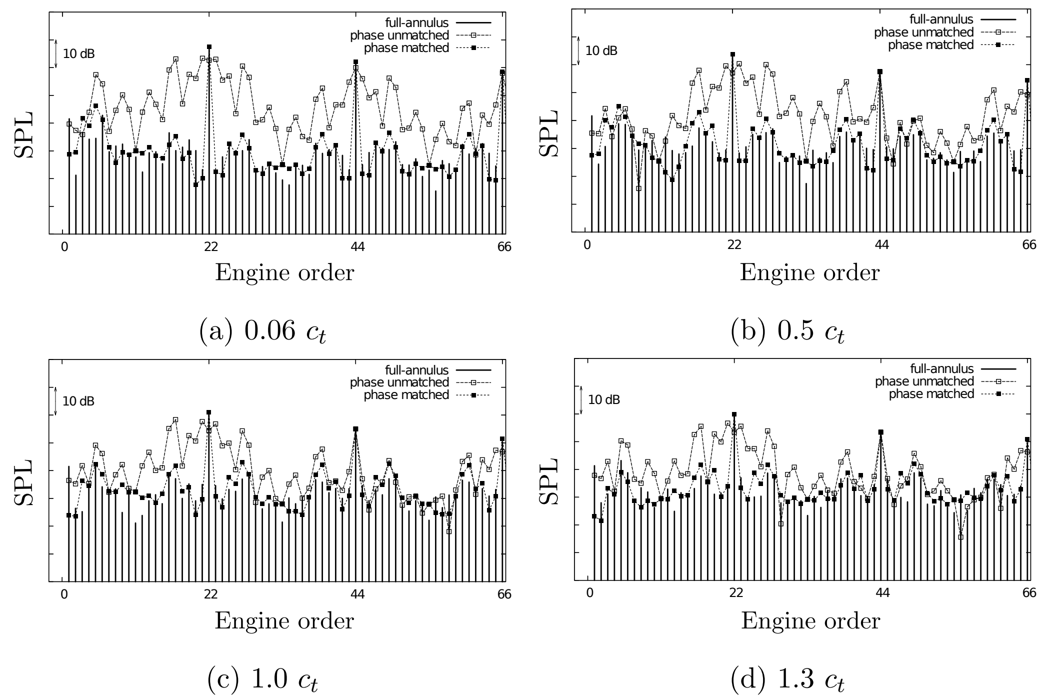


(a) 0.06 $c_t$

(b) 0.5 $c_t$

(c) 1.0 $c_t$

(d) 1.3 $c_t$

Figure 6: Validation of the linear superposition algorithm "superpose" against 2-D full-annulus simulations. Comparison presented for both phase-matched and phase unmatched results. Distance from the leading edge of the fan: (a) 0.06 $c_t$, (b) 0.5 $c_t$, (c) 1.0 $c_t$, and (d) 1.3 $c_t$ , where $c_t$ is the tip chord.

liner.

The two summation terms on the right hand side of Eq. 7 represent the nonlinear interaction between the tones. The second summation has to be truncated for numerical evaluation. The dissipation term $\epsilon$ in the equation accounts for the nonlinear dissipation that occurs at frequencies above the truncated limit. A method to estimate the value of $\epsilon$ by analyzing the dissipation rate in a regular sawtooth propagation was proposed in [9] and is used here. The adaptive-step Runge-Kutta scheme proposed by Cash and Karp [20] is used to integrate Eq. 7. For predicting MPT noise, the initial pressure spectrum is obtained using the linear superposition method described in the previous section.

The particular implementation of the pseudo 2-D model is validated against the analytical solution for evolution of a regular sawtooth wave by Morfey and Fisher [8]. For this validation exercise, the analytical spectrum at $T = 0$ is provided as initial condition to the nonlinear propagation code and the spectra at subsequent times is compared against analytical solution in Fig. 7.

### *4.1. Hardwall Duct*

For hardwall ducts, the liner dissipation term, $\sigma_m$ is set to zero for all $m$ and Eq. 7 is numerically integrated as described earlier. The 2-D full-annulus simulation described in Section 3 serves to further validate the accuracy of the pseudo 2-D non-linear propagation method. Spatial Fourier transform of the full-annulus CFD solution at the fan face provides the initial values of $C_m$. The linear superposition method to get the input values is not used for this validation exercise to avoid compounding of errors. Integration is then

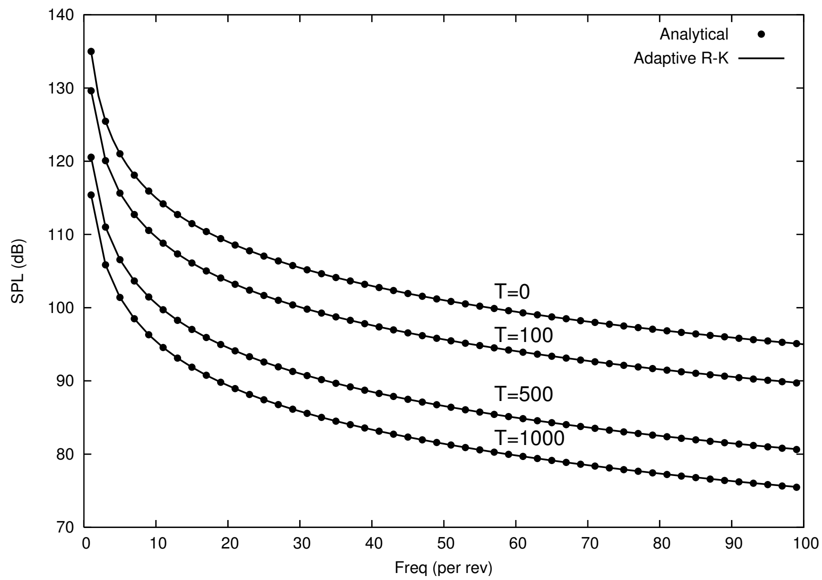


Figure 7: Evolution of the spectra of a regular sawtooth wave as predicted by the pseudo 2-D non-linear propagation model compared against analytical solution.

carried out to obtain $C_m$ at two different upstream axial locations, where they are compared against direct Fourier transform of the 2-D full annulus CFD solution. The comparison is shown in Fig. 8. The evolution of individual tones with upstream distance is also compared for four engine-order tones in Fig. 9, and BPF harmonics in Fig. 10. The model is able to capture the nonlinear evolution of engine-order as well as blade passing tone and their harmonics.

### *4.2. Lined Duct*

In-duct propagation of MPTs is also performed for lined ducts. Two approximations to represent the flow in the inlet duct are considered. The first assumes a plug (uniform) flow with no boundary layer, and in the second, a linear velocity profile is assumed in the boundary layer.

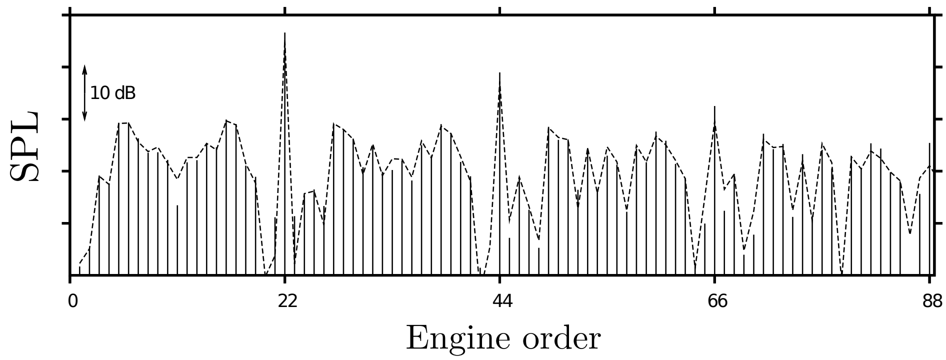


(a) 0.5 $c_t$ upstream of fan

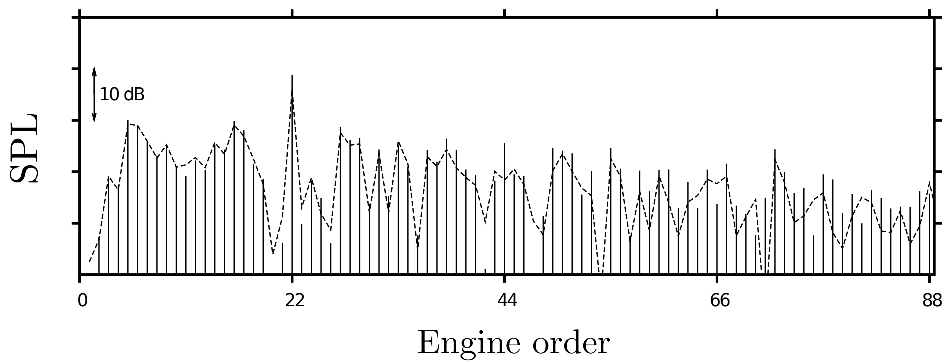


(b) 1.3 $c_t$ upstream of fan

Figure 8: Comparison of spectra predicted by the nonlinear model against those obtained from direct Fourier transform from the CFD solution at two axial distances upstream of the fan (a) 0.5 $c_t$ and (b) 1.3 $c_t$.

#### *4.2.1. Acoustic Attenuation Modeling*

*Uniform Flow Approach.* The attenuation factor, $\sigma_m$ in Eq. 7 is obtained by solving the classical eigenvalue problem of acoustic wave propagation in cylindrical ducts. For uniform flow in a cylindrical duct, the separation of variables technique is applied (in cylindrical-polar co-ordinates) to the convected wave equation (see e.g., Eversman [21]) to obtain the following

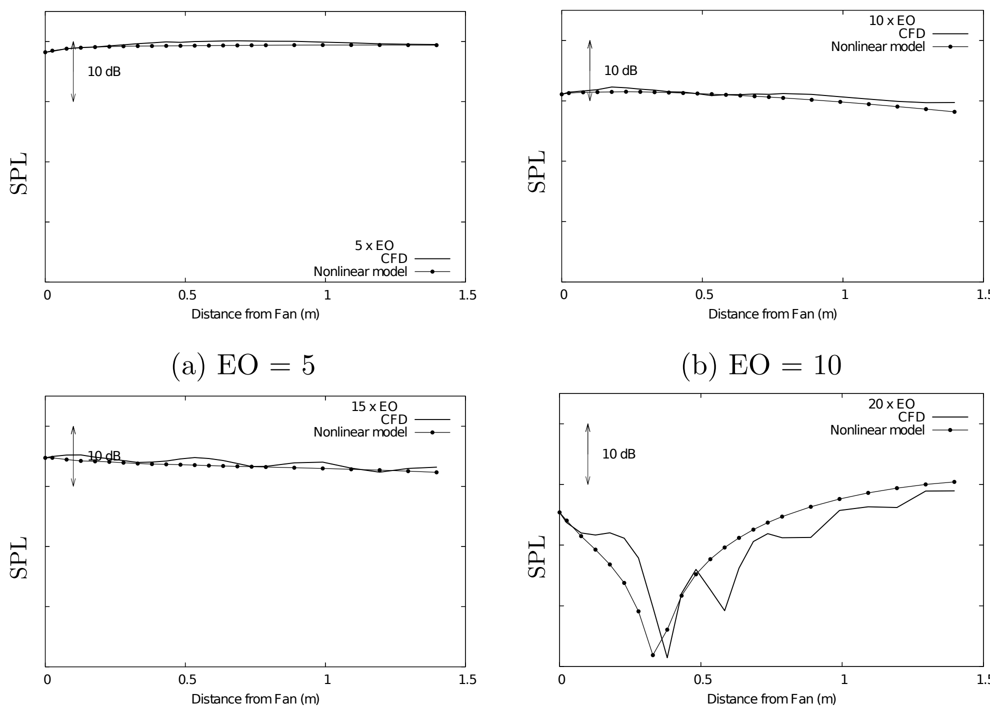


(a) EO = 5

(b) EO = 10

(c) EO = 15

(d) EO = 20

Figure 9: Comparison of evolution of four engine-order tones predicted by the nonlinear model against those obtained from direct Fourier transform from the CFD solution.

eigenvalue problem:

$$\frac{\mathrm{d}^2 P}{\mathrm{d}r^2} + \frac{1}{r}\frac{\mathrm{d}P}{\mathrm{d}r} + \left\{ \eta^2 \left[ \left(1 - M\frac{k_x}{\eta}\right)^2 - \left(\frac{k_x}{\eta}\right)^2 \right] - \frac{m^2}{r^2} \right\} P = 0. \tag{8}$$

In Eq. 8 $P$ is the acoustic pressure, $r$ is the radius normalized by the casing radius, $\eta$ is the non-dimensional frequency, $M$ is the absolute flow Mach number, and $k_x$ is the non-dimensional axial acoustic wavenumber. For soft wall ducts, the acoustic boundary condition at r=1 is

$$\left.\frac{\mathrm{d}P}{\mathrm{d}r}\right|_{r=1} = -i\eta A \left(1 - M\frac{k_x}{\eta}\right)^2 P, \tag{9}$$

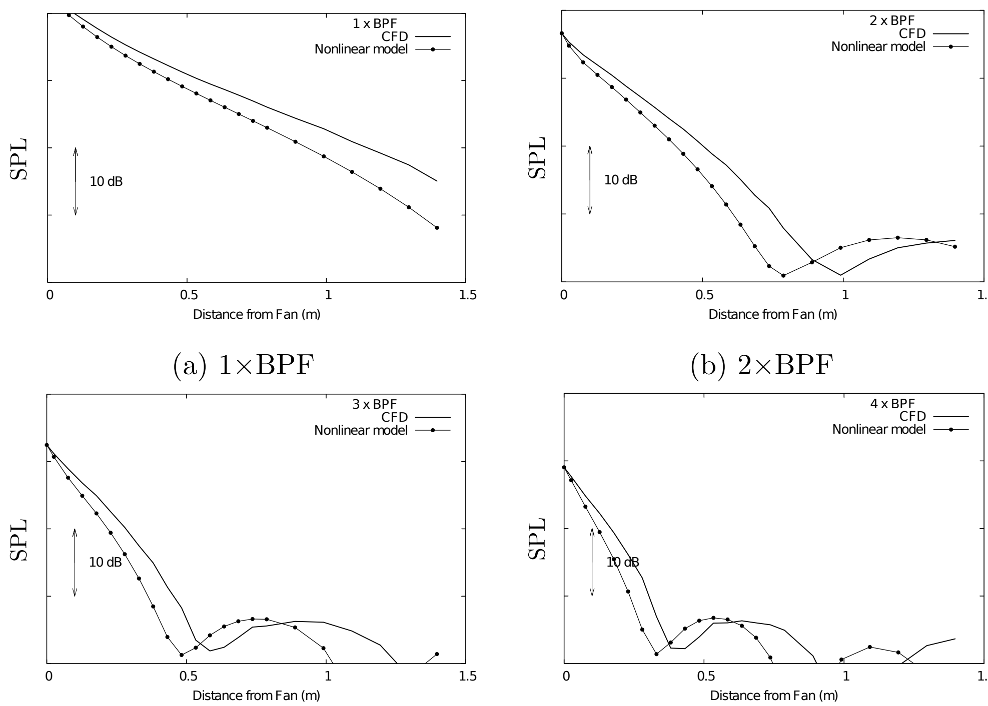


(a) 1×BPF

(b) 2×BPF

(c) 3×BPF

(d) 4×BPF

Figure 10: Comparison of evolution of first four harmonics of the blade passing fundamental tone between the prediction by the nonlinear model against those obtained from direct Fourier transform from CFD solution.

where $A$ is the acoustic admittance of the liner normalized by $\rho_0 c$. In the cylindrical duct case, the radial acoustic pressure variation is represented by Bessel functions of the first kind, denoted here by $J_m$. The eigenvalue equation then becomes

$$\kappa \frac{J_m'(\kappa)}{J_m(\kappa)} = -i\eta A \left(1 - M\frac{k_x}{\eta}\right)^2, \tag{10}$$

with

$$\frac{k_x}{\eta} = \frac{1}{1-M^2}\left[-M \pm \sqrt{1-(1-M^2)\left(\frac{\kappa}{\eta}\right)^2}\,\right], \tag{11}$$

where, $\kappa$ is the non-dimensional radial wavenumber. Equations 10 and 11 are solved together for the axial wavenumber, $k_x$. The imaginary part of $k_x$, which represents damping due to acoustic liner, is used to compute $\sigma_m$ (required for use in Eq. 7) using the "time of flight" [8] relation as follows:

$$\sigma_m = Im\{k_x\}\,\frac{2\pi r_{tip}}{B}\,\frac{\sqrt{M_{rel}^2-1}}{M_{rel}^4}\times\left(M_a\sqrt{M_{rel}^2-1}-M_t\right)^2. \tag{12}$$

In above, $k_x$ is the axial wave number for the $m^{th}$ mode, $B$ is number of fan/rotor blades, $r_{tip}$ is the fan/rotor tip radius, $M_{rel}$ is the blade relative flow Mach number, $M_t$ is the blade tip Mach number, and $M_a$ is the axial flow Mach number.

*Effect of Boundary Layer on Liner Attenuation.* The assumption of uniform mean flow was used in deriving Eqs. 8 and 9. In reality, fluid viscosity along with the no slip boundary condition at the wall produces a boundary layer and in general the flow is radially non-uniform. Assuming that the meanflow is only along the axial direction in a cylindrical duct, the linearized Euler equations reduce to the Pridmore-Brown [22] equation and can be written for a single frequency, single mode in the Fourier-wavenumber space as

$$\frac{\mathrm{d}^2P}{\mathrm{d}r^2}+\left[\frac{1}{r}+\frac{2k_x}{\eta-Mk_x}\frac{\mathrm{d}M}{\mathrm{d}r}\right]\frac{\mathrm{d}P}{\mathrm{d}r}+\left\{\eta^2\left[\left(1-M\frac{k_x}{\eta}\right)^2-\left(\frac{k_x}{\eta}\right)^2\right]-\frac{m^2}{r^2}\right\}P=0. \tag{13}$$

The boundary condition at the wall is specified as

$$\left.\frac{\mathrm{d}P}{\mathrm{d}r}\right|_{r=1}=-i\eta AP. \tag{14}$$

Ideally, the attenuation factor $\sigma_m$ in the nonlinear code should be obtained by solving the eigenvalue problem given by Eqs. 13 and 14. However, these are difficult to solve for a mean flow with physically accurate boundary layers. For cases where the boundary layer is thin compared to the duct radius, Eversman [23] produced an asymptotic approach that uses Eq. 13 for axial propagation with an equivalent boundary condition that is enforced at the edge of the boundary layer. This equivalent boundary condition is

$$\left.\frac{\mathrm{d}P}{\mathrm{d}r}\right|_{r=1} = -\frac{(1-M_0K)^2\left\{i\eta A + \delta\left[\beta\int_0^1 \mathrm{d}\xi/(1-M_0K\phi)^2 - \alpha\right]\right\}}{1+i\delta\eta A\int_0^1(1-M_0K\phi)^2\mathrm{d}\xi}P, \quad (15)$$

where, $\delta$ is the boundary layer thickness normalized by the duct radius, $M_0$ is the core mean flow Mach number, $K = k_x/\eta$, $\alpha = \eta^2 - i\eta A$, and $\beta = m^2 + \eta^2K^2$. The velocity profile in the boundary layer is given by

$$M(\xi) = M_0\phi(\xi), \quad 0 \le \xi \le 1, \quad (16)$$

where $\xi = 1$ corresponds to the outer edge of the boundary layer. As expected, when $\delta = 0$, Eq. 15 reduces to Eq. 9, the boundary condition for the case of uniform mean flow. Myers and Chuang [24] improved upon the asymptotic approach and obtained

$$\begin{aligned}\left.\frac{\mathrm{d}P}{\mathrm{d}r}\right|_{r=1} &= -i\eta A(1-M_0K)^2P \\ &- \delta\left[\kappa^2 - m^2 + \kappa^2\frac{J_m'^2(\kappa)}{J_m^2(\kappa)}\left(1-\int_0^1\frac{h(\xi)}{h_0}\mathrm{d}\xi\right) - h_0\int_0^1\frac{h(\xi)-k_x^2-m^2}{h(\xi)}\mathrm{d}\xi\right]P, \quad (17)\end{aligned}$$

where $h(\xi) = (\eta - k_xM_0\phi(\xi))^2$. Note that when $\delta = 0$, Eq. 17 also reduces to Eq. 9 of the uniform mean flow case. Myers and Chuang [24] compared this approach with the one by Eversman [23] and showed that their approach improved the accuracy for thicker boundary layers. Equations 8 and 17 are used in the present analyses to solve for the eigenvalues and hence the attenuation factor, $\sigma_m$ is obtained. The boundary layer is assumed to have a linear profile (see Fig. 11 (a)). Figure 11 (b) plots the attenuation per unit axial distance as a function of boundary layer thickness for five engine orders.

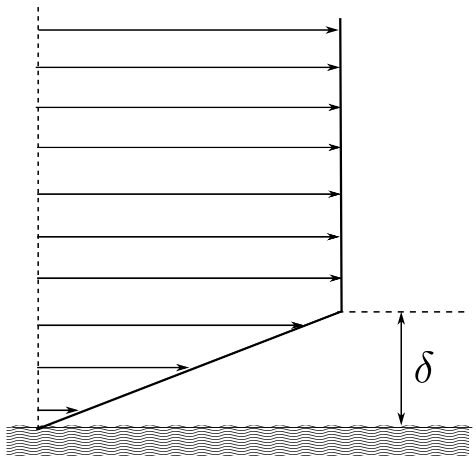


(a) Assumed boundary layer profile

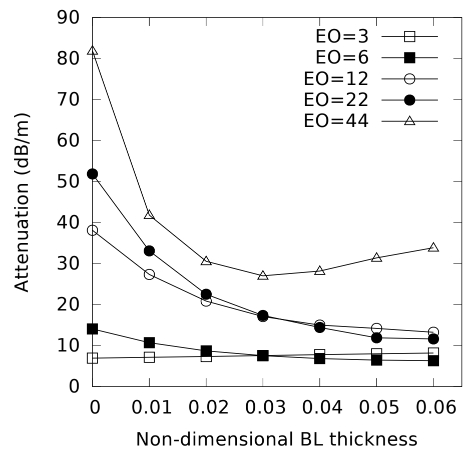


(b) Attenuation effect

Figure 11: Impact of boundary layer thickness, $\delta$ on the attenuation factor: (a) assumed linear boundary layer profile and (b) attenuation per unit length for engine orders $3, 6, 12, 22$, and $44$.

For the mode with azimuthal order 3 (EO=3), boundary layer thickness does not show much effect on the axial attenuation of the mode. As the mode order is increased, the boundary layer effect becomes more significant. This can be explained by comparing the duct mode shapes for different azimuthal orders in Fig. 12. As the azimuthal order of the mode increases, its mode shape, and hence acoustic energy, gets weighted more and more towards the casing. Hence the impact of the boundary layer on liner attenuation increases with increasing mode order. Figure 12 compares first radial duct mode shapes for uniform flow (hardwall) with duct mode shapes for flow with $\delta = 0.03$. The lower order modes (e.g., $m = 3, 6$) show little difference between uniform flow case and that with a boundary layer. Perceptible difference is seen only for the highest mode order ($m = 22$) attempted here.

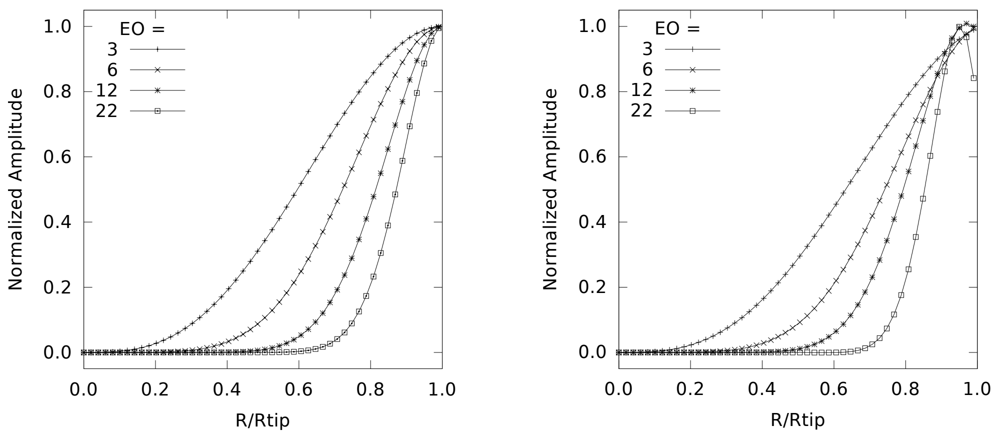


(a) Hardwall, uniform flow

(b) Lined wall, $\delta = 0.03$

Figure 12: A comparison between first radial order modes for (a) hardwall with no boundary layer and (b) lined wall with $\delta = 0.03$.

## 5. Step #3: Far Field Radiation

Due to nonlinear dissipation as well as liner attenuation (if present), MPT noise decays inside nacelle with upstream distance. As the wavefronts leave the waveguide (duct), their amplitudes are expected to reduce much faster due to wave expansion in 3-D. The pseudo 2-D propagation method cannot deal with wave propagation outside the cylindrical duct as the governing equation (Eq. 7) needs to be modified to include 3-D expansion as well as to account for the modification in the characteristic direction of the waves. A linear model that can handle both in-duct as well as 3-D propagation outside the duct is therefore used to propagate noise to the farfield. ACTRAN/TM, a numerical code developed by Free Field Technologies, is employed for these linear simulations. ACTRAN/TM solves for the perturbed (acoustic) field over a pre-computed time-averaged irrotational flowfield. The irrotational meanflow is calculated using the commercial flow solver CFX. The CFX meanflow is matched to the TACOMA result by driving the CFX calculation to push the same massflow through the inlet duct. ACTRAN/TM solutions are carried out using either a full 3-D domain, or a 2-D, axisymmetric flow approximation.

The transition from the nonlinear model to the linear model is performed close to the nacelle lip. The choice of the transition location should theoretically be determined by measuring the variation of tone amplitudes with upstream distance. In hardwall configurations, it is sometimes difficult to choose a location inside the engine nacelle that satisfies this criterion. Therefore, an axial plane closest to the inlet duct is chosen. For lined configurations, pressure waves attenuate rapidly inside the nacelle, so the transition location is chosen such that the entire liner is modeled using the pseudo 2-D propagation method.

The output of the pseudo 2-D nonlinear propagation is acoustic pressure spectrum inside the duct near the casing at the transition location. It is assumed that the pressure pattern stays rotor locked (one azimuthal order per frequency) and that all the acoustic energy is concentrated in the first radial mode. Since the transition location is chosen where there is no liner, and the first radial modes for a hardwall duct have peak pressure at the casing (see Fig. 12 a), the output of the nonlinear propagation code directly gives the peak modal pressure amplitudes. Hardwall mode shape and modal amplitude are taken as input in the ACTRAN simulation subsequently to compute scattering from nacelle lip and far-field radiation. Note that in the input to ACTRAN, all the acoustic energy in the $m^{th}$ engine order tone is assumed to be in the $[m, 0]$ (first radial) mode. It should be further clarified that in reality, the flow near the nacelle lip will be non-uniform and the duct mode shapes will be slightly different from those computed for uniform flow in a cylinder. We expect that the error introduced by this approximation is small.

## 6. Comparison against Static Engine Test Data

The prediction approach described above is applied to predict MPT noise from a typical high bypass ratio engine during a static engine test. The surface coordinates of each blade are measured using a coordinate measuring machine (CMM) and decomposed into eigenmodes. The amplitude of the eigenmode corresponding to stagger is used to estimate the stagger angle of each blade. As-measured stagger angles of the fan blades thus obtained are used with the prediction methodology. The reader should note the following approximation implicitly made here - the CMM measured coordinates are for a "cold" blade; when running ("hot"), the blade shape changes (mostly it un-twists) due to centrifugal and aerodynamic loads. It is assumed that the stagger variations stay the same between "cold" and "hot" conditions.

All the results in this paper are at the operating condition where the axial flow Mach number in the inlet duct, $M_a = 0.52$ and fan blade tip Mach number, $M_t = 1.027$. The Helmholtz number (based on duct radius) for the blade passing tone is $He = 22.65$. Comparisons with experimental data are made for the following measurements: unsteady surface pressure measurements (two transducers) in the inlet duct, and two microphone arrays - (1) a straight-line arc in the near-field, and (2) a circular arc at a distance of approximately 14 fan diameter from the engine center. The locations of the transducers, relative to the fan blade leading edge, are shown in Fig. 13 (a). The locations of the near- and far-field microphones, relative to the engine center, are shown in Fig. 14. Both hardwall and lined-wall configurations are considered. For the lined-wall case, two liner configurations in the engine inlet were tested, referred to here as liner A and liner B. Sketches showing the axial locations of liners A and B are shown in Fig. 13.

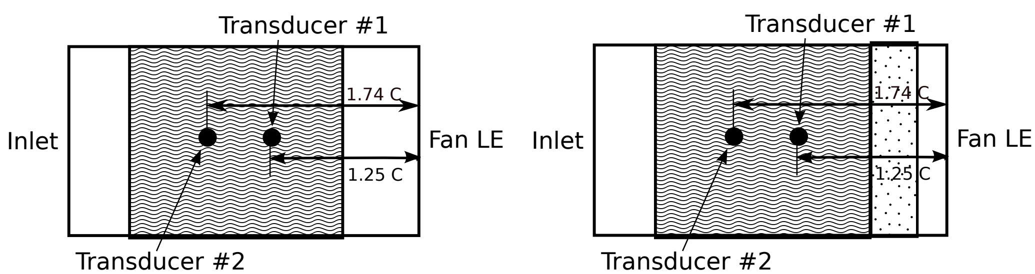


(a) Liner A

(b) Liner B

Figure 13: Schematic showing the location of the transducers as well as the two liner (shaded areas) configurations used in static engine tests and predictions. The location of transducers is the same between hardwall and lined experiments.

### *6.1. In-Duct Wall Pressure Comparison*

The linear superposition algorithm (described in Section 3) is applied using as-measured blade stagger angles to compute the MPT spectrum just upstream of the fan. The MPTs are then propagated upstream using the pseudo 2-D nonlinear propagation method described in Section 4. The results

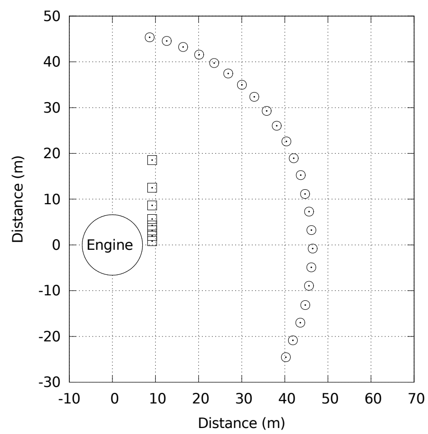


Figure 14: Microphone array locations in the static engine tests. Squares denote near-field microphone locations and circles denote far-field microphone locations.

for the hardwall configuration are presented in Fig. 15 (a) and (b), which compare the predicted and the measured spectra at transducers #1 and #2 respectively. There is little difference between the spectra at the two transducers because of the relatively small distance between them and due to the absence of liner in the hardwall case. Nevertheless, both the data and the predictions exhibit the same behaviour and the absolute comparison is found to be acceptable.

The same approach is employed for the lined-wall cases. In the nonlinear propagation using the pseudo 2-D method, liner attenuation is modeled using the parameter $\sigma_m$. Two flow cases are considered: (1) plug flow, and (2) flow with a linear velocity profile in the boundary layer. The effect of the boundary layer is modeled using the Myers-Chuang approach described in Section 4. The ratio of the boundary layer height to the casing radius is fixed at 0.025 for all the computations presented here. This value is obtained using the results from a few CFD calculations which are not described here

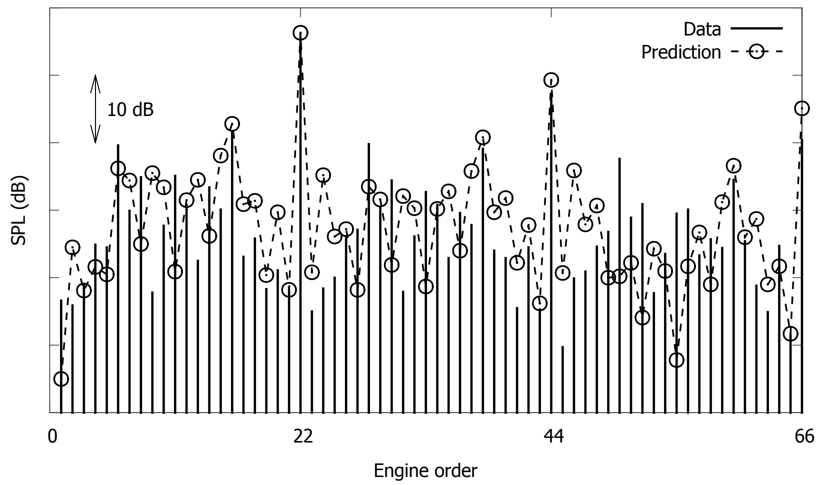


(a) Transducer #1

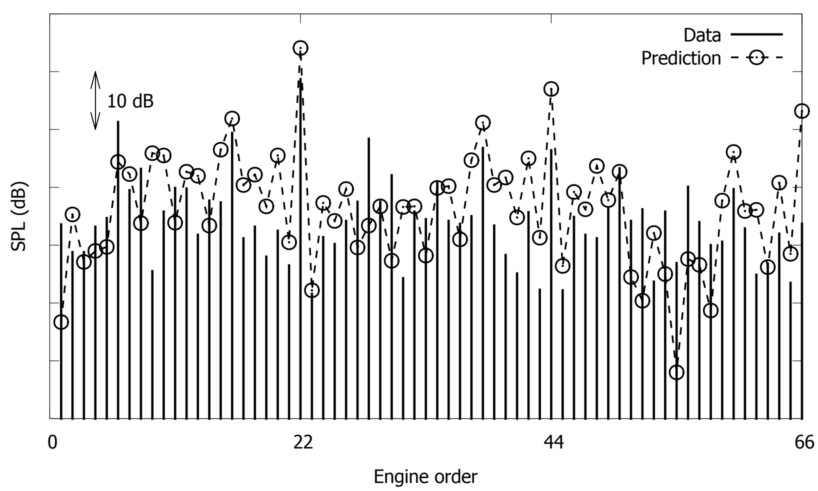


(b) Transducer #2

Figure 15: Comparison of hardwall spectra between the predictions and the measurements at the two transducer locations shown in Fig. 13.

for brevity. The measured and the predicted sound pressure levels at the transducer #1 location are shown in Fig. 16, for the two liner configurations.

The importance of modeling the effect of the boundary layer is highlighted by the significant overprediction (particularly for the high-order modes) of liner attenuation with the plug flow assumption. The liner attenuation is captured well for both liner configurations when the boundary layer effect is modeled using the Myers-Chuang approach.

### *6.2. Near- and Far-field Microphone Comparisons*

MPTs are associated with rotor-locked pressure patterns that rotate at the shaft rotation rate. Each MPT frequency therefore has a fixed azimuthal mode order. For the geometry and inflow conditions considered, the tones with engine orders 1 through 5 are expected to decay exponentially because their frequencies fall below the "cut-off" threshold. Therefore, only the tones with engine order greater than 6 are evaluated. ACTRAN/TM is used to simulate the near-to-far-field propagation, which is carried out either as a 2-D axisymmetric calculation, or a full 3-D calculation. The grid requirement as well as the computation time increase tremendously with the frequency (mode order) and hence the full 3-D simulations are limited to the sub-BPF (engine order $< 22$) tones. Tones with engine orders up to 66 (or $3\times$ BPF) are simulated using the 2-D axi-symmetric flow approximation. For brevity, only the results for the liner configuration B are presented. Prediction accuracy is found to be similar for liner configuration A.

Spectra between the data and the predictions are compared at the polar angle (measured from upstream) equal to 50 degrees. Figures 17 and 18 compare the measured and the predicted SPL spectra at the near- and the far-field microphones for hardwall and liner B configurations respectively. The relatively small difference between the spectra from the ACTRAN 3-

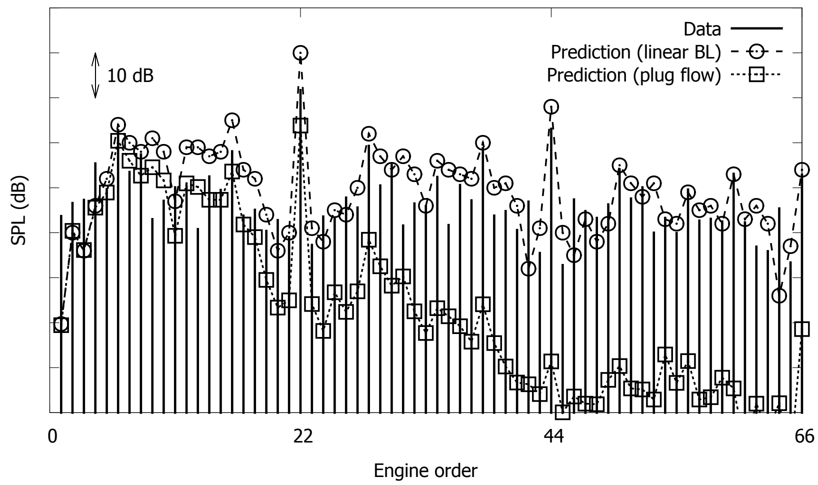


(a) Liner A

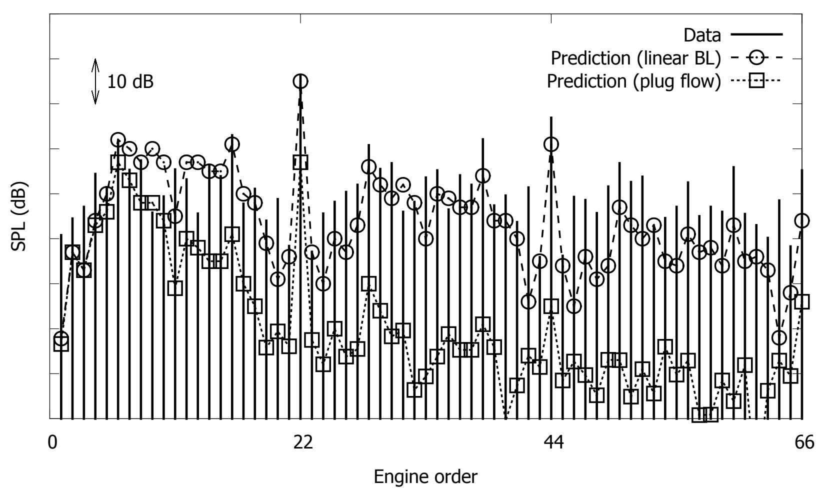


(b) Liner B

Figure 16: Measured and predicted MPT spectrum at the transducer #1 location for the static engine test for (a) liner A, and (b) liner B configuration.

D model versus the ACTRAN 2-D axisymmetric model for engine orders 622 suggests that the 2-D axi-symmetric model is sufficient for the geometry under consideration. Also, considering the fidelity of the other steps in the prediction process, the 3-D radiation model is perhaps unnecessarily complex. The standard deviation between the measured and the predicted results (between the hardwall and the lined-wall configurations) for all engine orders is around 10 dB.

Directivity comparisons at the near- and the far-field microphone array locations for tones with engine orders 6 and 12 are made for both hardwall (Figs. 19 and 20) and liner B (Figs. 21 and 22) configurations. Both the 3-D as well as the 2-D axi-symmetric ACTRAN/TM models capture the measured data reasonably well. The 2-D axi-symmetric flow approximation gives slightly lower SPLs at small angles in the far-field. This is due to its inability to model 3-D geometry and mean flow scattering effects in the linear propagation and radiation process. The full 3-D solution is slightly better, even so, it also under-predicts the measured SPLs at small angles, particularly in the far-field. For axisymmetric inlet and flow, all acoustic duct modes (except for the planar mode) have a null along the engine axis. The 2-D axi-symmetric model predicts zero (to machine precision) acoustic pressure along the engine axis. The 3-D model accounts for the inlet droop. Due to this deviation from axi-symmetry, exact cancellation does not occur along engine axis in the 3-D model and hence the predicted power is slightly higher. The prediction from the 3-D model still falls significantly short of the measured SPL near engine axis. There are several potential reasons for this: (1) multi-modal sources (e.g., broadband noise), (2) scattering of MPT noise in lower circumferential orders during generation or propagation (as will happen in the case of non-axisymmetric inlet, spliced liners, etc.), which

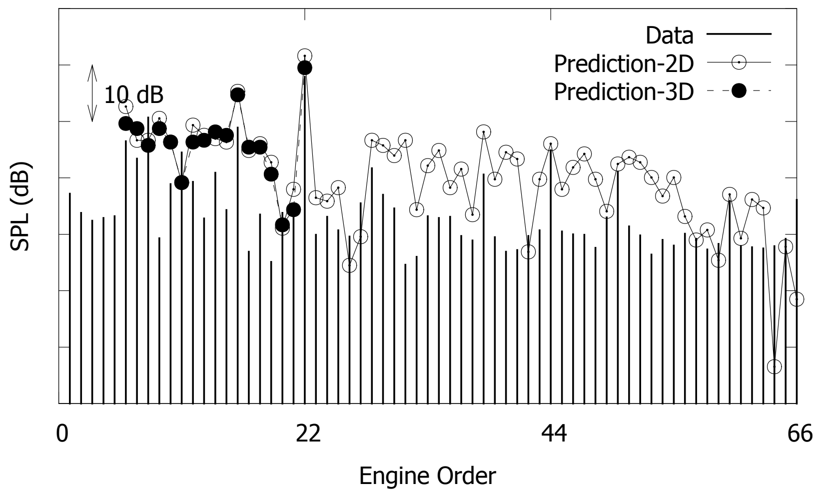


(a) Near-field

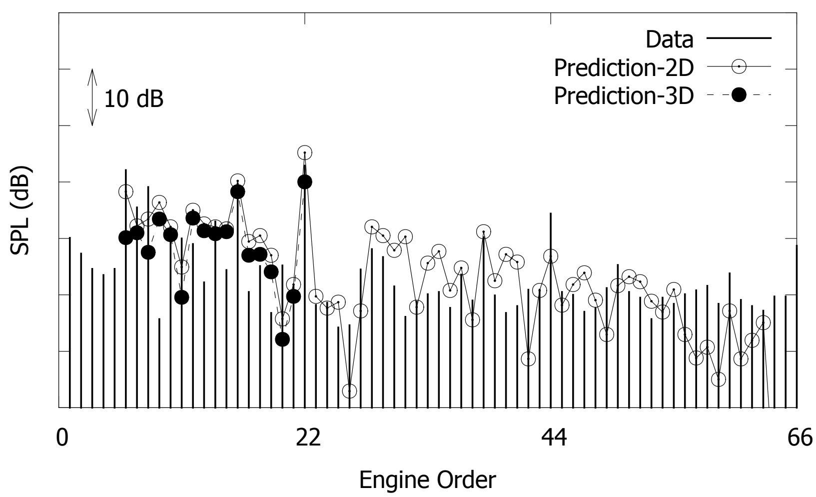


(b) Far-field

Figure 17: Measured and predicted MPT SPL spectra at (a) near-field and (b) far-field at the $50^0$ microphone for the static engine test case, for the hardwall configuration.

is not modeled, and (3) facility noise.

It should be noted that the pseudo 2-D nonlinear propagation method

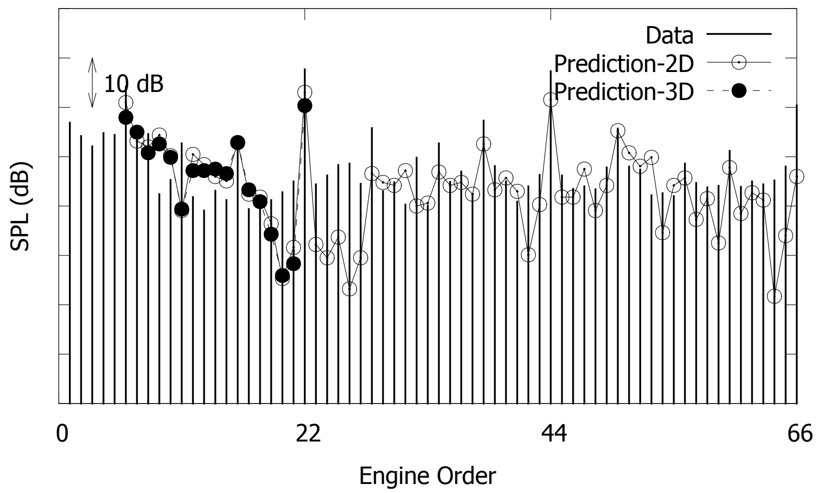


(a) Near-field

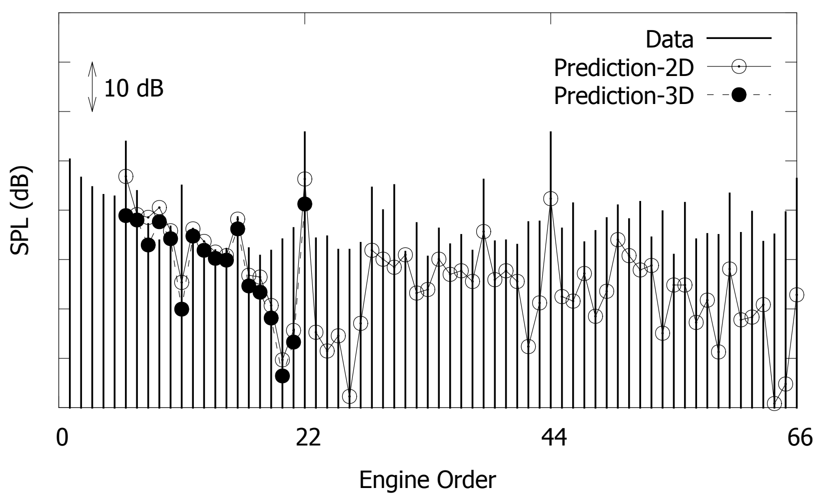


(b) Far-field

Figure 18: Measured and predicted MPT SPL spectra at (a) near-field and (b) far-field at the $50^0$ microphone for the static engine test case, for the Liner B configuration.

employed here constrains all the acoustic energy per frequency in one duct mode - the lowest radial mode. In reality, due to non-axisymmetric geometry, meanflow, and liner (when present), scattering of acoustic energy into multiple azimuthal and radial modes is inevitable. The inability to model this scattering in the pseudo 2-D propagation method is a drawback. However, the speed and the simplicity of the model make it a good design software.

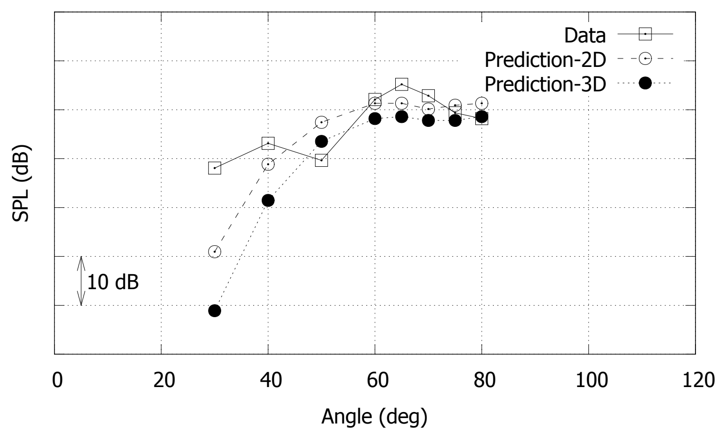


(a) Near-field

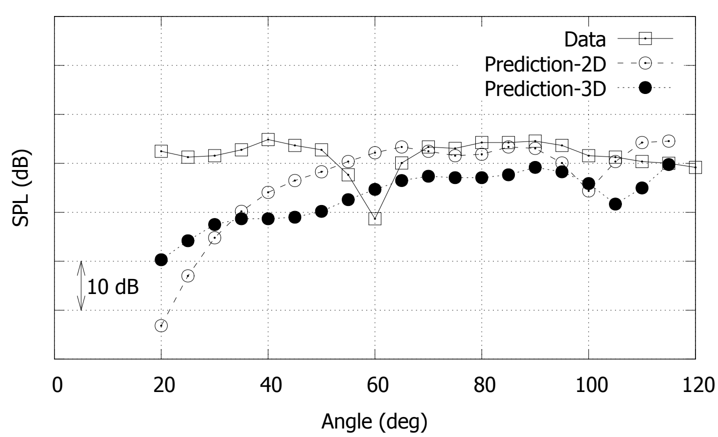


(b) Far-field

Figure 19: Measured and predicted MPT SPL directivity at (a) near-field microphone array and (b) far-field microphone array for the static engine test case, EO= 6, for the hardwall configuration.

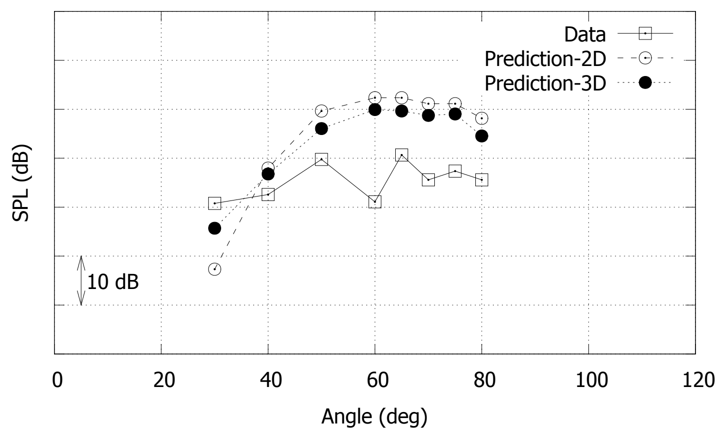


(a) Near-field

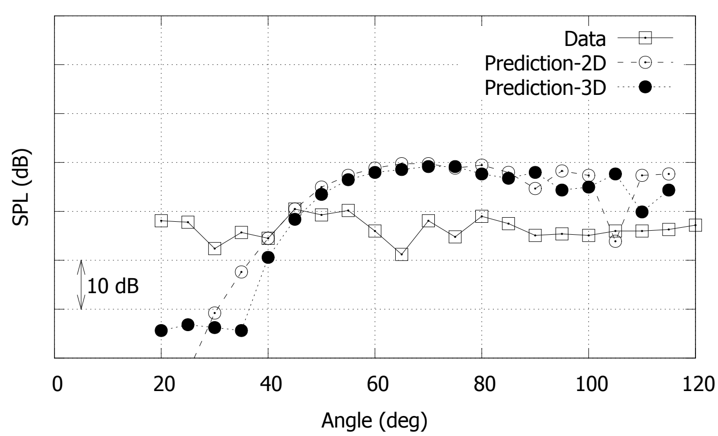


(b) Far-field

Figure 20: Measured and predicted MPT SPL directivity at (a) near-field microphone array and (b) far-field microphone array for the static engine test case, EO= 12, for the hardwall configuration.

### *6.3. Trend Predictions*

The fundamental goal of a noise prediction software is to guide the designer to low-noise designs. To assess the predictive capability of this numerical procedure in differentiating designs, the spectral data is reduced to

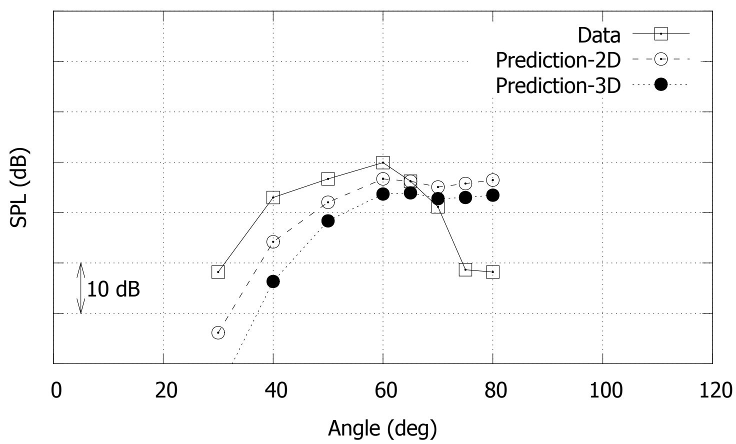


(a) Near-field

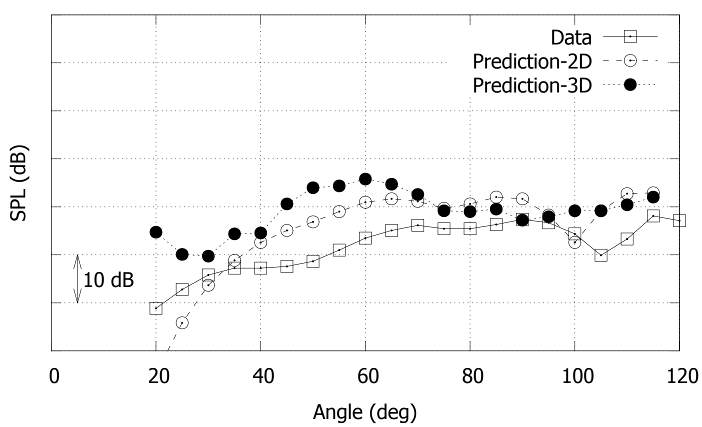


(b) Far-field

Figure 21: Measured and predicted MPT SPL directivity at (a) near-field microphone array and (b) far-field microphone array for the static engine test case, EO= 6, for the Liner B configuration.

a scalar overall sound power level (OAPWL) number. The OAPWL is calculated for the hardwall, the liner A, and the liner B configurations and is obtained as follows. First, the measured MPT SPL spectra between the polar angles $50^0$ and $80^0$ are averaged to obtain an averaged MPT spectrum. The

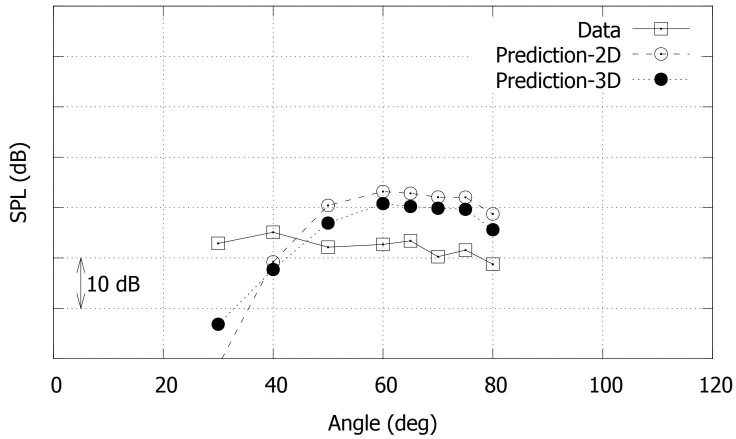


(a) Near-field

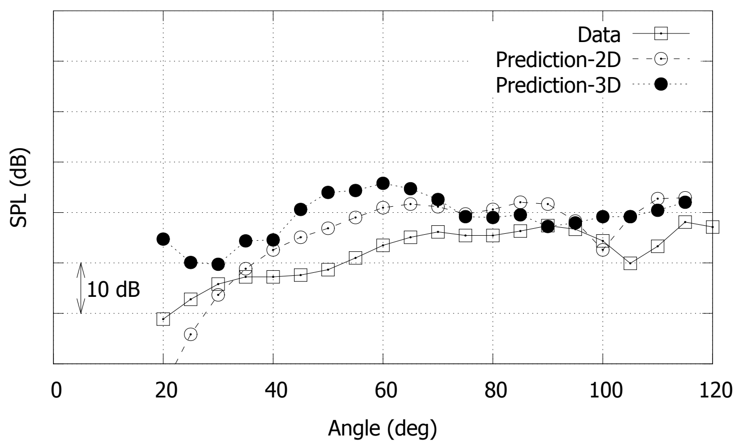


(b) Far-field

Figure 22: Measured and predicted MPT SPL directivity at (a) near-field microphone array and (b) far-field microphone array for the static engine test case, EO= 12, for the Liner B configuration.

acoustic power in each tone (from engine order 1 through 66) is then added to obtain the overall sound power level (OAPWL). Both the measured and the predicted results are reduced in the same manner. Note that only the MPT tones (including the blade passing harmonics) are considered in computing the PWL sum (referred loosely as OAPWL here). Figure 23 shows the OAPWL trend between the hardwall, liner A, and liner B configurations. For all three configurations, the trend is predicted correctly and the absolute levels for the measured and the predicted OAPWL are within 4 dB. The additional noise reduction of around 2.5 dB for liner B over liner A is also predicted correctly.

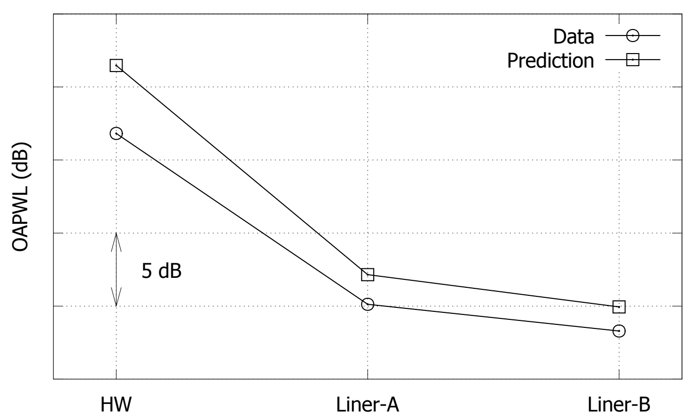


Figure 23: Measured and predicted MPT OAPWL for the static engine test case.

## 7. Conclusions

A numerical procedure to predict the generation, in-duct propagation, and far-field radiation of MPT noise for hardwall and acoustically treated aero-engine inlets is described. The procedure consists of three steps. First, part-annulus RANS CFD simulations are carried out to generate the pressure field upstream of the fan blades. A linear superposition method is used with measured fan blade stagger angle distribution to construct the circumferentially non-uniform pressure field (MPTs) for the full bladerow just upstream of the fan. This pressure distribution is then used in the second step as an input to a pseudo 2-D non-linear propagation model to investigate the propagation of MPT from just upstream of the fan blades to the nacelle lip. In the final step, ACTRAN/TM is used for linear acoustic mode propagation and radiation from the nacelle lip to the far-field.

The proposed prediction methodology is applied to a typical high bypass ratio engine during a static engine test and comparisons are made for hardwall as well as two acoustically treated inlets. Comparisons are drawn against measured unsteady surface pressure data on the inlet casing and against noise spectra from microphones in the near- and the far-field. The predictions are found to be in reasonable agreement with the measured data. Sound pressure levels at small angles to the engine axis are underpredicted. The prediction process is found to be accurate in predicting overall noise power level trends between hardwall to lined-wall, and between two liner configurations.

## 8. Acknowledgment

The authors would like to express their appreciation for the many useful discussions with Muni Majjigi, Richard Cedar, and Bryan Callender at GE Aviation, as well as John Premo and Cyrille Breard at the Boeing Company.

## References

[1] B. S. Stratford, D. R. Newby, A new look at the generation of buzz-saw noise, AIAA 77-1343.

[2] P. Gliebe, R. Mani, H. Shin, B. Mitchell, G. Ashford, S. Salamah, S. Connel, Aeroacoustic prediction codes, NASA/CR–2000-210244.

[3] M. G. Philpot, The buzz-saw noise generated by a high duty transonic compressor, ASME Paper No. 70-GT-54.

[4] D. L. Hawkings, Multiple tone generation by transonic compressors, Journal of Sound and Vibration 17 (2) (1971) 241–250.

[5] M. Kurosaka, A note on multiple tone noise, Journal of Sound and Vibration 19 (4) (1971) 453–462.

[6] M. R. Fink, Shock wave behavior in transonic compressor noise generation, ASME Paper No. 71-GT-7.

[7] G. F. Pickett, Prediction of the spectral content of combination tone noise, Journal of Aircraft 9 (9) (1972) 658–663.

[8] C. L. Morfey, M. J. Fisher, Shockwave radiation from a supersonic ducted rotor, The Aeronautical Journal of the Royal Aeronautical Society 74 (1970) 579–585.

[9] A. McAlpine, M. J. Fisher, On the prediction of “buzz-saw” noise in aero-engine inlet ducts, Journal of Sound and Vibration 248 (1) (2001) 123–149.

[10] A. McAlpine, M. J. Fisher, On the prediction of “buzz-saw” noise in acoustically lined aero-engine inlet ducts, Journal of Sound and Vibration 265 (1) (2003) 175–200.

[11] A. McAlpine, M. J. Fisher, B. J. Tester, “Buzz-saw” noise: A comparison of measurement with prediction, Journal of Sound and Vibration 290 (3-5) (2006) 1202–1233.

[12] A. McAlpine, P. J. G. Schwaller, M. J. Fisher, B. J. Tester, "buzz-saw" noise: Prediction of the rotor-alone pressure field, Journal of Sound and Vibration 331 (22) (2012) 4901–4918.

[13] S. Uelleberg, Buzzsaw noise prediction for modern turbofans, AIAA 2004-3000.

[14] L. Xu, Shockwave and noise abatement of transonic fans, ASME Paper No. GT2004-53545.

[15] D. Prasad, J. Feng, Propagation and decay of shock waves in turbofan engine inlets, ASME Paper No. GT2004-53949.

[16] R. Schnell, Investigation of the tonal acoustic field of a transonic fanstage by time-domain cfd-calculations with arbitrary blade counts, ASME Paper No. GT2004-54216.

[17] ACTRAN User's Manual.

[18] D. G. Holmes, B. E. Mitchell, C. B. Lorence, Three dimensional linearized navier-stokes calculations for flutter and forced response, in: Proceedings of the 8th ISUAAT Symposium, Stockholm, Sweden, 1997.

[19] M. Nyukhtikov, N. Smelova, B. E. Mitchell, D. G. Holmes, Optimized dual-time stepping technique for time-accurate navier-stokes calculations, in: Proceedings of the 14th ISUAAT Symposium, Duke University, 2003.

[20] J. R. Cash, A. H. Karp, A variable order runge-kutta method for initial

value problems with rapidly varying right-hand sides., ACM Transactions on Mathematical Software 16 (2) (1990) 201–222.

[21] W. Eversman, Theoretical models for duct acoustic propagation and radiation, in: H. H. Hubbard (Ed.), Aeroacoustics of Flight Vehicles: Theory and Practice, NASA Langley Research Center, Hampton, Virginia, 1991, pp. 165–206.

[22] D. C. Pridmore-Brown, Sound propagation in a fluid flowing through an attenuating duct, Journal of Fluid Mechanics 4 (4) (1958) 393–406.

[23] W. Eversman, Approximation for thin boundary layers in the sheared flow duct transmission problem, The Journal of the Acoustical Society of America 53 (5) (1973) 1346–1350.

[24] M. K. Myers, S. L. Chuang, Uniform asymptotic approximations for duct acoustic modes in a thin boundary-layer flow, AIAA Journal 22 (9) (1984) 1234–1241.